Research Square

Preprints are preliminary reports that have not undergone peer review.
They should not be considered conclusive, used to inform clinical practice,
or referenced by the media as validated information.

Na exospheric emission in relation to Sun events during the BepiColombo Second Mercury's Fly-by

Anna Milillo

anna.milillo@inaf.it

INAF https://orcid.org/0000-0002-0266-2556

Mirko Stumpo

INAF, Institute of Space Astrophysics and Planetology

Valeria Mangano

INAF, Institute of Space Astrophysics and Planetology

Alessandro Mura

INAF/IAPS https://orcid.org/0000-0002-4552-4292

Ali Varsani

Space Research Institute, Austrian Academy of Sciences https://orcid.org/0000-0003-1814-1568

Daniel Heyner

Technische Universität Braunschweig

Daniel Schmid

Space Research Institute, Austrian Academy of Sciences https://orcid.org/0000-0001-7818-4338

Stas Barabash

Swedish Institute of Space Physics

Lina Hadid

Laboratoire de Physique des Plasmas (LPP), CNRS-Observatoire de Paris-Sorbonne Université-Université Paris Saclay-Ecole polytechnique-Institut Polytechnique de Paris https://orcid.org/0000-0002-8587-0202

Nicolas André

IRAP, SUPAERO

Emilia Kilpua

University of Helsinki https://orcid.org/0000-0002-4489-8073

Rami Vainio

University of Turku https://orcid.org/0000-0002-3298-2067

Pier Paolo Di Bartolomeo

INAF, Institute of Space Astrophysics and Planetology

Stefano Massetti

INAF-Istituto di Astrofisica e Planetologia Spaziali https://orcid.org/0000-0002-7767-1334

Martina Moroni

INAF, Institute of Space Astrophysics and Planetology

Mathias Rojo

IRAP

STEFANO ORSINI

Institute of Space Astrophysics and Planetology, INAF https://orcid.org/0000-0002-5588-1920

Sebastien Verkercke

Laboratoire de Physique des Plasmas (LPP), CNRS-Observatoire de Paris-Sorbonne Université-Université Paris Saclay-Ecole polytechnique-Institut Polytechnique de Paris

Hayley Williamson

Swedish Institute of Space Physics https://orcid.org/0000-0003-0071-2342

Sae Aizawa

LPP, CNRS https://orcid.org/0000-0002-3483-3444

Alessandro Aronica

IAPS-INAF https://orcid.org/0000-0003-3205-9472

Wolfgang Baumjohann

Space Research Institute, Austrian Academy of Sciences https://orcid.org/0000-0001-6271-0110

Alessandro Brin

INAF

Dragos Constantinescu

Institut für Geophysik und Extraterrestrische Physik, Technische Universität Braunschweig, Braunschweig, Germany.

Elisabetta De Angelis

INAF

Dario Del Moro

University of TorVergata

Willi Exner

Max Planck Institute for Solar System Research

David Fischer

Space Research Institute, Austrian Academy of Sciences, Graz, Austria

Harald Jeszenszky

Austrian Academy of Sciences

Adrian Kazakov

INAF

Norbert Krupp

Max Planck Institute for Solar System Research https://orcid.org/0000-0003-4683-9533

Gunter Laky

Space Research Institute, Austrian Academy of Sciences

Cristina Leto

ASI

Stefano Livi
University of Michigan
Ayako Matsuoka
Kyoto University https://orcid.org/0000-0001-5777-9711
Hans Nilsson
Swedish Institute of Space Physics
Denise Perrone
Agenzia Spaziale Italiana https://orcid.org/0000-0003-1059-4853
Christina Plainaki
INAF
Jim Raines
University of Michigan, Department of Climate and Space Sciences and Engineering
https://orcid.org/0000-0001-5956-9523
Ingo Richter
TU Braunschweig https://orcid.org/0000-0002-5324-4039
Rosanna Rispoli
INAF
Yoshifumi Saito
JAXA https://orcid.org/0000-0002-1354-3544
Roberto Sordini
Institute of Space Astrophysics and Planetology, INAF https://orcid.org/0000-0002-2242-6147
Nello Vertolli
INAF

Article

Keywords: Mercury, exosphere, Mercury-Sun interaction, multi messenger observations

Posted Date: November 10th, 2026

DOI: https://doi.org/10.21203/rs.3.rs-11364478/v1

License: This work is licensed under a Creative Commons Attribution 4.0 International License.
Read Full License

Additional Declarations: There is **NO** Competing Interest.

Na exospheric emission in relation to Sun events during the BepiColombo Second Mercury's Fly-by

Anna Milillo[1*†], Mirko Stumpo[1†], Valeria Mangano[1†], Alessandro Mura[1], Ali Varsani[2], Daniel Heyner[3], Daniel Schmid[2], Stas Barabash[4], Lina Z. Hadid[5], Nicolas André[6,7], Emilia Kilpua[8], Rami Vainio[9], Pier Paolo Di Bartolomeo[1], Stefano Massetti[1], Martina Moroni[1], Mathias Rojo[6], Stefano Orsini[1], Sebastien Verkercke[5], Hayley Wiliamson[4], Sae Aizawa[5], Alessandro Aronica[1], Wolfgang Baumjohann[2], Alessandro Brin[1], Dragos, O. Constantinescu[3,16], Elisabetta De Angelis[1], Dario Del Moro[10], Willi Exner[11], David Fischer[2], Harald Jeszenszky[2], Adrian Kazakov[1], Norbert Krupp[11], Gunter Laky[2], Cristina Leto[12], Stefano Livi[13], Ayako Matsuoka[14], Hans Nilsson[4], Denise Perrone[12], Christina Plainaki[1], Jim, M. Raines[13], Ingo Richter[3], Rosanna Rispoli[1], Yoshifumi Saito[15], Roberto Sordini[1], Nello Vertolli[1]

[1*]IAPS, INAF, via del Fosso del Cavaliere 100, Rome, 00133, Italy.
[2]Space Research Institute, Austrian Academy of Sciences, Graz, Austria.
[3]Institute for Geophysics and Extraterrestrial Physics, TU Braunschweig, Braunschweig, Germany.
[4]Swedish Institute of Space Physics, Kiruna, Sweden.
[5]LPP, Ecole polytechnique, CNRS, Sorbonne Université, Université Paris Saclay, Observatoire de Paris, Paris-Saclay, France.
[6] Institut de Recherche en Astrophysique et Planétologie (IRAP, CNRS-CNES-Université de Toulouse, Toulouse, France.
[7]Institut Supérieur de l'Aéronautique et de l'Espace (ISAE-SUPAERO), Université de Toulouse, Toulouse, France.
[8]Department of Physics, University of Helsinki, Helsinki, Finland.
[9]Department of Physics and Astronomy, University of Turku, Turku, Finland.
[10], University of TorVergata, Rome, Italy.
[11]Max Planck Institute for Solar System Research, Göttingen, Germany.

[12]ASI - Italian Space Agency, Rome, Italy.
[13]Department of Climate and Space Sciences and Engineering,University of Michigan, Ann Arbor, MI, USA.
[14]World Data Center for Geomagnetism, Graduate School of Science, Kyoto University, Kyoto, Japan.
[15]Institute of Space and Astronautical Science, Japan Aerospace Exploration Agency, Sagamihara, Japan.
[16]Institute of Space Science - INFLPR Subsidiary, Măgurele, Romania.

*Corresponding author(s). E-mail(s): anna.milillo@inaf.it;
Contributing authors: mirko.stumpo@inaf.it; valeria.mangano@inaf.it;
†These authors contributed equally to this work.

Abstract

During BepiColombo second Mercury's flyby on 23 June 2022, a ground-based campaign with the THEMIS solar telescope provided simultaneous observations of the sodium (Na) exosphere while Bepicolombo measured interplanetary and magnetospheric conditions. Between 8:53 and 9:34 UT, the exospheric Na emission abruptly increased in intensity by about 70% across the entire day side, followed by a slow recovery to the preceding level over approximately four hours. BepiColombo did not register neither relevant perturbations of the solar wind nor solar energetic particles during the Na increase. The configuration of Mercury, Earth and Solar Orbiter enabled observations of the solar regions facing Mercury from both sides. They revealed that an active region facing Mercury, but hidden from Earth, produced a flare and an extreme-ultraviolet (EUV) brightening when the Na emission increased, whereas subsequent emissions from post-flare loops produced no further increase. While photon-stimulated desorption is one of the main mechanisms releasing Na from the surface, short-therm Na variability has so far been attributed mainly to plasma precipitation. Our observations suggest that solar flares can trigger rapid Na variability at Mercury, and point to a multi-phase release from a finite reservoir of surface sodium, reminiscent of the steeper than linear dependence on solar EUV reported for the Moon on longer timescales. This result marks a significant step forward in understanding the mechanisms governing the interaction of Mercury and the Moon with the Sun and it was possible thanks to multi-messenger observations highlighting the potential of investigations during BepiColombo nominal mission.

Keywords: Mercury, exosphere, Mercury-Sun interaction, multi messenger observations

1 Introduction

Sodium is a common constituent of rocky planetary surfaces in the Solar System and beyond, including moons and asteroids, from which it can be ejected into the surrounding exospheres and atmospheres. At airless bodies, sodium release from the surface to the exosphere provides a particularly important diagnostic tool, as the ejected material is more directly exposed to the external environment. However, its release is caused by multiple agents and processes, making the Na exosphere more complex to characterize than for other species [1, 2]

In particular, Mercury's Na exosphere exhibits seasonal variations on timescales of months [e.g. 3, 4] as well as short term variations occurring on timescales ranging from hours to tens of minutes [e.g. 5, 6]. Different surface release mechanisms of Na atoms could be temporarily or locally more efficient depending first on external conditions - such as interplanetary magnetic field (IMF), the solar wind, the illumination and the micrometeoroid flux - that are highly variable along Mercury's eccentric orbit [1, 2, 7–9], secondly on surface properties such as regolith porosity, composition, mineralogy, and temperature [e.g. 10, 11]. Photons in the UV energy range interact with the upper surface and subsequently stimulate the desorption of excited component states (Photon Stimulated Desorption process - PSD). Solar wind ions impacting the surface produce both particle release by ion-sputtering process and surface alteration by chemical sputtering and space weathering processes. Although the impinging ions have enough energy to break the bonds of Na in the surface minerals, the sputtering yield is not sufficient to account for the observed intensity of the Na exosphere [12]. Conversely, UV photons do not have enough energy to liberate Na atoms bound in surface minerals (> 5 eV) [10], but efficiently release Na atoms that are only physically bound to the surface of the mineral, i.e., atoms already detached from the mineral bonds (< 2.7 eV) [10, 13]. The general picture is therefore that on Mercury's day side, intense fluxes of ions and photons can impinge on the same surface cell, producing enhanced Na release [14, 15].

Double mid-latitude enhancements are generally attributed to plasma precipitation at the footprint of the magnetospheric cusps [e.g. 16–18]) and are expected to exhibit short time variability. To robustly establish a link between ion impact and Na release, global and local observations of Na exosphere from ground-based telescopes and space based instruments would greatly benefit from in-situ information of the external conditions. During MErcury Surface, Space ENvironment, GEochemistry, and Ranging (MESSENGER) mission (2011-2015 [19]), the few occasions of simultaneous observations with the THEMIS solar telescope allowed joint analysis of Na exosphere variability in relation to IMF conditions [18]. One of these was a fortunate case when MESSENGER in-situ observations registered two interplanetary Coronal Mass Ejections (ICMEs) impinging on Mercury [6]. These authors documented a Na exosphere evolving from a distribution with two peaks at mid-latitudes to an intensification centered close to the equatorial region. Between the two ICMEs a decrease of emission was registered, and finally a new intensification was observed during the second ICME passage at Mercury. This behavior was attributed to the compression of the magnetopause close to the surface due to the enhanced dynamic pressure of the ICMEs, allowing their plasma to impact the entire day side.

At the Moon, long-term variations of the Na exosphere have been correlated with the solar EUV and FUV emission (from 256 to 1405 Å) [20]. Photons above 8.8 eV exceed the binding energies of Na in the minerals, and, according the authors, EUV and FUV photons are able to produce a non-thermal release process, likely PSD, at energies higher (up to 6000 K) than the energies obtained by previous estimations (1200 K) [21]. By correlating the Na emission with each solar band separately, that study found a steeper than linear increase of the Na abundance with the EUV and FUV flux, in contrast with the linear relation derived in the laboratory for photons above 4 eV (i.e <3000 Å) [21].

The role of solar flares in this picture is unexplored. Flares enhance the solar X-ray and EUV irradiance within minutes, by factors that grow with photon energy (e.g., [22]), and at Mercury this radiation is much more intense than at Earth. Testing their effect on the exosphere is, however, observationally difficult because the irradiance reaching Mercury comes from the solar hemisphere facing the planet, which in general is only partially visible from Earth.

The six Mercury Flybys of the ESA-JAXA cornerstone mission BepiColombo [23] gave the opportunity to obtain direct measurements of the IMF, solar wind and Mercury's magnetosphere. When possible, the Flybys also provided valuable occasions to perform simultaneous ground-based observations during dedicated campaigns of THEMIS solar telescope [24]. In particular, the second Mercury Flyby (MFB2, 23 June 2022) provided a unique opportunity for joint analysis during an extraordinarily variable Na exosphere. Here we report a detailed analysis of the increase of Mercury's Na exosphere observed by THEMIS in the full Earth-facing illuminated portion. We give an overview of the plasma conditions at Mercury as observed by BepiColombo. Combining observations of the Sun from Earth and from Solar Orbiter, which together covered the solar hemisphere facing Mercury, we are able to register the Sun activity toward Mercury. All these observations provide important indications for defining the release mechanisms that could explain Na dynamics.

2 Results

During MFB2 on 23 June 2022, when Mercury was at a true anomaly angle (TAA) of 263° (heliocentric distance 0.38 AU), BepiColombo ran inbound from dusk in the far tail. The closest approach, 200 km of altitude, was at 9:44 UT in pre-dawn sector. The outbound was into the dawn sector of the day side. The trajectory started in the southern hemisphere in a nearly equatorial path as shown in Fig. 1. The instruments were operational from 22 to 25 June 2022.

The ground-based campaign from the THEMIS solar telescope took place from 23 June 2022 at 6:30 until 30 June afternoon [24]. As reported in this paper, the Na emission exhibited an interesting variability in both intensity and distribution throughout the campaign. The observations on the MFB2 day are listed in 1. Starting from a single-peak configuration on 23 June 2022 at 6:30 UT, distributed over the whole illuminated day side (Fig. 2), Na emission abruptly increased with its intensity almost doubling (+70%) as registered by the image acquired between 8:53 and 9:34 UT on 23 June 2022. This increase coincided with the time when BepiColombo passed

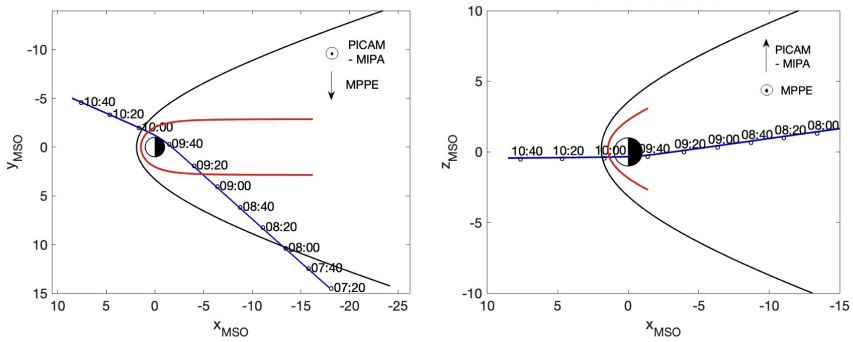


Fig. 1 BepiColombo second flyby trajectory (blue line) in xMSO-yMSO plane (left) and in xMSO-zMSO plane (right). The labels along the blue curve report the time in UT of the spacecraft. In the two plots the red curves show the magnetopause [25] and the black curves show the average bow-shock of Mercury magnetosphere [26]. The arrows point to the boresight directions of SERENA-PICAM and -MIPA ion sensors and indicate MPPE look direction

into Mercury's magnetosphere. The image taken between 9:40 and 10:30 UT suffered from bad pointing and cannot be used in the data analysis, but the subsequent images taken when BepiColombo was exiting to the upstream solar wind showed a gradual decrease in Na emission; at 12:46 UT the emission went back to the initial intensity and configuration in full Earth-facing illuminated portion. Along the following days, the distribution changed again exhibiting the characteristic double peak distribution [24]. The obvious and naive interpretation of this abrupt variability is that it could be related to the presence of an ICME or another kind of extreme event, similar to observations by Orsini et al. [6]. However, in such a case, BepiColombo should have registered a clear signature of strong ion precipitation across the entire day side, like intense dynamic pressure of the solar wind or detection of planet-ward ion fluxes.

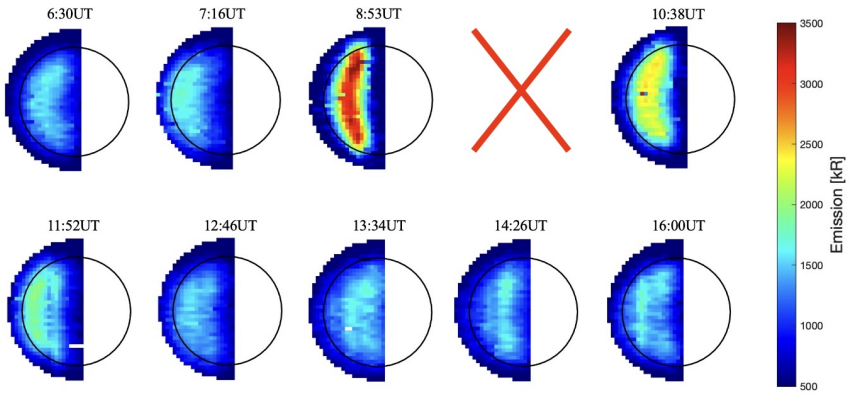


Fig. 2 Sequence of THEMIS ground-based observations during 23 June 2022, the day of the second Mercury flyby. The time indicates the start time of the acquisition. The gap between 8:53 and 10:38 UT shows that an image has been disregarded due to bad quality.

Table 1 List of Na exospheric observations with THEMIS on June 23, 2022. During observations TAA was 264-266 degrees and Phase Angle 87-86 degrees.

Id. Nr.	Time range of observation (UT)	Seeing (")	Quality factor (Q)
t005	06:30 - 07:11	1.75	1.0
t007	07:16 - 07:57	2.00	1.0
t011	08:53 - 09:34	1.00	0.9
t016	10:38 - 11:19	1.00	1.0
t022	11:52 - 12:34	1.75	0.3
t024	12:46 - 13:27	2.00	0.5
t026	13:34 - 14:15	2.00	0.3
t028	14:26 - 15:07	2.00	0.5
t035	16:00 - 16:41	1.75	0.3

In Fig. 3, observations of the solar wind and IMF before and after the crossing of Mercury's magnetosphere are shown. The solar wind observed by SERENA-PICAM (from now on PICAM) shows a high variability both in energy and intensity. Note that the intensity observed by PICAM can vary according to the sensor orientation. In fact, PICAM Field of View (FoV) is a wide cone of about 160° with the boresight perpendicular to the Sun direction. The solar wind can enter more/less favorably when the spacecraft velocity is anti-parallel/parallel to the boresight for aberration effects. This means that the long-term variability of the intensity observed by PICAM could be due to the spacecraft orientation. In contrast, short-term variations (less than tens of minutes) are due to real solar wind fluctuations [27]. According to the MERMAG magnetic field data (Fig. 3a), both before and after the flyby, the IMF intensity was approximately stable, but the orientation showed some rotation (in y- and z Mercury Solar Orbital - MSO components) producing oscillations between positive (North) and negative (South) IMF. The solar wind was quite stable with an average velocity slowly decreasing in time from about 430 km/s to 370 km/s. The conditions upstream and downstream are summarized in Table 2 (updated from Rojo et al. [28], Teubenbacher et al. [29]).

Table 2 Downstream and upstream conditions during the BepiColombo MFB2

Averaged parameters	inbound	outbound	unit
IMF magnitude	30	25	nT
Solar wind energy	950	700	eV
Solar wind velocity	430	370	km/s
Solar wind estimated density	35-40	45-50	cm^{-3}
Solar wind pressure	11	10	nPa
Alfvén velocity	110	80	km/s
Alfvén M_A	3.9	4.5	

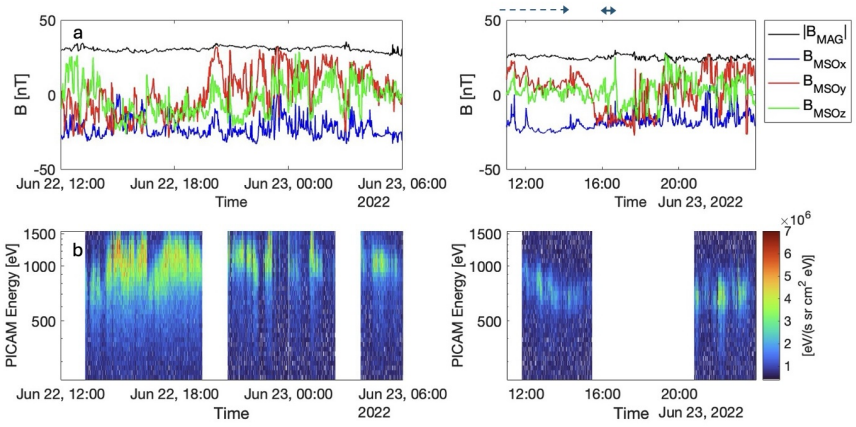


Fig. 3 (a) Magnetic field measurements from MERMAG and coordinates in Mercury Solar Orbit (MSO) reference frame and (b) Differential energy ion fluxes by PICAM while BepiColombo was approaching Mercury from downstream (left) and after the spacecraft exited the bow-shock (right). The arrows above show the periods when THEMIS images have been collected in the two plotted intervals.

In Fig. 4 the measurements obtained by BepiColombo during the MFB2 magnetospheric crossing are shown. From the magnetic field intensities obtained by joint analysis of the MERMAG magnetometers, the inbound bow shock and magnetopause crossing can be identified at 7:50 and 9:10 UT, respectively, in agreement with MPPE-MEA (from now on MEA) observations reported in Rojo et al. [28]. These boundaries are also supported by the PICAM observations showing a simultaneous decrease in energy while entering the magnetosheath and a decrease in ion intensity while entering inside the magnetosphere. The signature of an active reconnection region in Mercury's magnetotail has been identified by combined analysis of magnetic field, ion and electron measurements [30].

Between 9:35 and 9:50 UT close to the closest approach in the post-midnight/dawn region, the ion energies measured by SERENA-MIPA (from now on MIPA) and PICAM reached up to 14 keV and electron energy observed by MEA up to 3 keV. These high energies are an indication of active magnetosphere, as suggested by Williamson et al. [31]. According to these authors, the ions at energy > 1 keV are freshly injected particles in the loss cone. This population could be the signature of plasma convected and energized from the tail [32]. Because of large artificial disturbances during the eclipse complete cleaning of the magnetic field cannot be achieved around the closest approach [33] (see Section 5.2.3). Electrons with energies above 100s eV are observed by MEA as transient pulses showing energy-time dispersed features supporting the interpretation of the occurrence of multiple substorm-related injections, similar to those registered during MFB1 [34]. It is difficult to estimate whether these particles could precipitate toward the surface of the planet, but it is clear that they cannot account for an intense and abrupt ion precipitation across the whole day side [35, 36].

In the day side, the magnetopause outbound boundary was clearly identifiable at 9:52 UT as an increase of the plasma densities [28], and an increase in magnetic

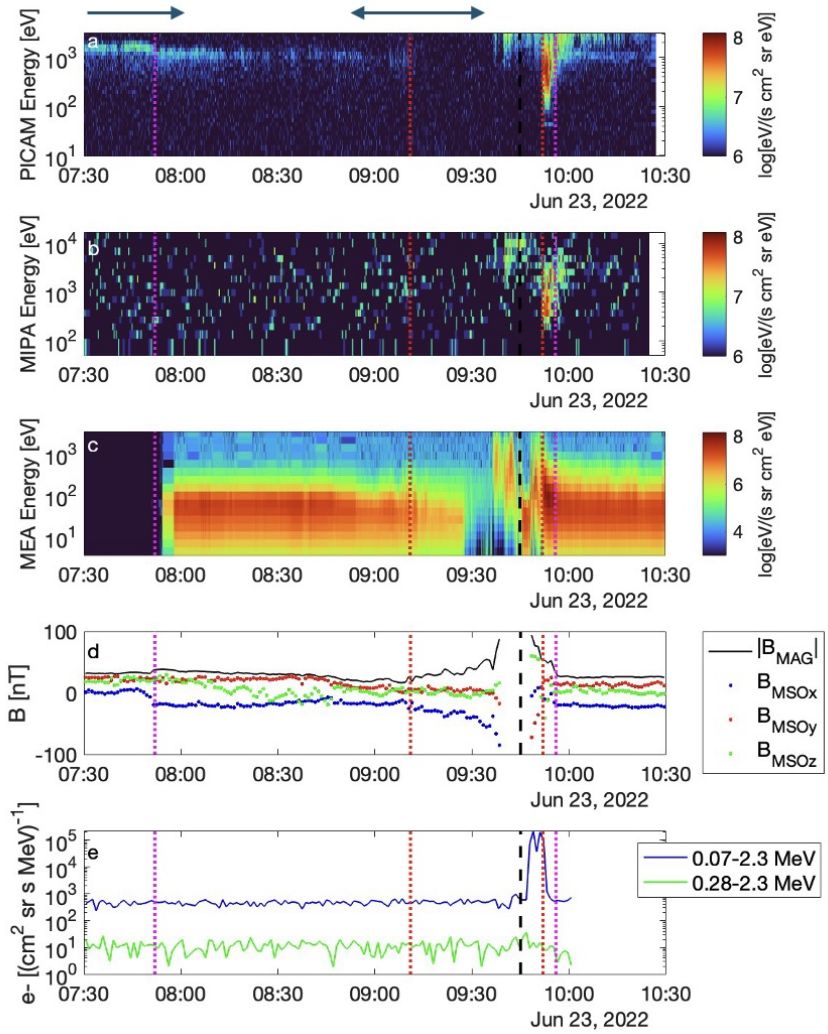


Fig. 4 BepiColombo observations during the MFB2. a) and b) Differential energy omnidirectional ion fluxes by SERENA ion sensors PICAM and MIPA, respectively. c) Electron differential fluxes by MEA1. d) Magnetic field intensity and MSO components observed by MERMAG. Note that artificial magnetic disturbances prevent obtaining clean magnetic field measurements during eclipse. e) SIXS-P electron observation in two energy channels. Magnetopause crossings are shown as dotted red lines, bow-shock crossings are shown as magenta dotted lines and closest approach is shown as dashed black line. The arrows above show the THEMIS observation intervals in the plotted period.

field fluctuations. The bow shock crossing was not clearly discernible in either the ion or magnetic field data; however, the signature of a dynamic boundary was observed

between 09:55 and 09:57 UT. In contrast, the electron data revealed a distinct transition at 9:56:42 UT [28]. Upstream of the bow shock, foreshock ions have been observed by PICAM and MIPA in agreement with the quasi-parallel IMF configuration [37].

While BepiColombo was exiting from the planet shadow at 9:46 UT, SIXS observed an increase in electron fluxes in the energy range 70-280 keV, but there was no evidence of energetic protons. This electron event features relatively soft spectra, more typical of the magnetospheric population than of energetic particles of solar origin. Unfortunately, in situ day side measurements are not available when the exospheric emission increase was observed by THEMIS. If an intense electron flux occurred when the spacecraft was behind the planet, a possible increase of Na release could be due to electron stimulated desorption. However, this process is not expected to be relevant with respect to the PSD in the day side [38, 39].

In summary, despite the quite active magnetosphere during the investigated flyby, we cannot identify a specific particle precipitation event simultaneously to the ground-based observation enhancement, especially one that could involve the whole day side and be so intense that it could produce the doubling of the Na release.

As mentioned in section 1, Na surface release may be induced not only by particle impact onto the surface, but also by UV photons [8, 9, 20]. We therefore examined the solar emission directed towards Mercury during MFB2. On 23 June 2022, Mercury was at Stonyhurst longitude W71 and 0.378 au from the Sun, while Solar Orbiter was at W159 (1.006 au), 159° from the Sun–Earth line (Fig. 5a). This configuration allowed SDO (Earth view) and Solar Orbiter to observe from opposite sides the solar longitudes facing Mercury (Fig. 5b,c respectively; dimmed areas are not visible from Mercury). All times are given as observed by each instrument. The increase in Na emission therefore started between 07:57 and 08:53 UT, i.e., between the end of exposure t007 and the start of t011, and the brightest image (t011) covers 08:53–09:34 Mercury time.

We identified a brightening of an active region (AR) located at W106S33 (Fig 5a). The AR was in full view from Mercury (47° from the sub-Mercury point) and from Solar Orbiter, but 14° behind the west limb as seen from Earth. From Earth, therefore, only the coronal emission above about 23-Mm was visible, as the off-limb brightening in the south-west quadrant of the SDO/AIA images (Fig. 5b). The EUI images show the AR on the disk (Fig. 5c), and STIX X-ray imaging places in the same region the sources of the peaks observed at 08:13, 09:39, 09:55 and 11:03 UT (Fig. 5f).

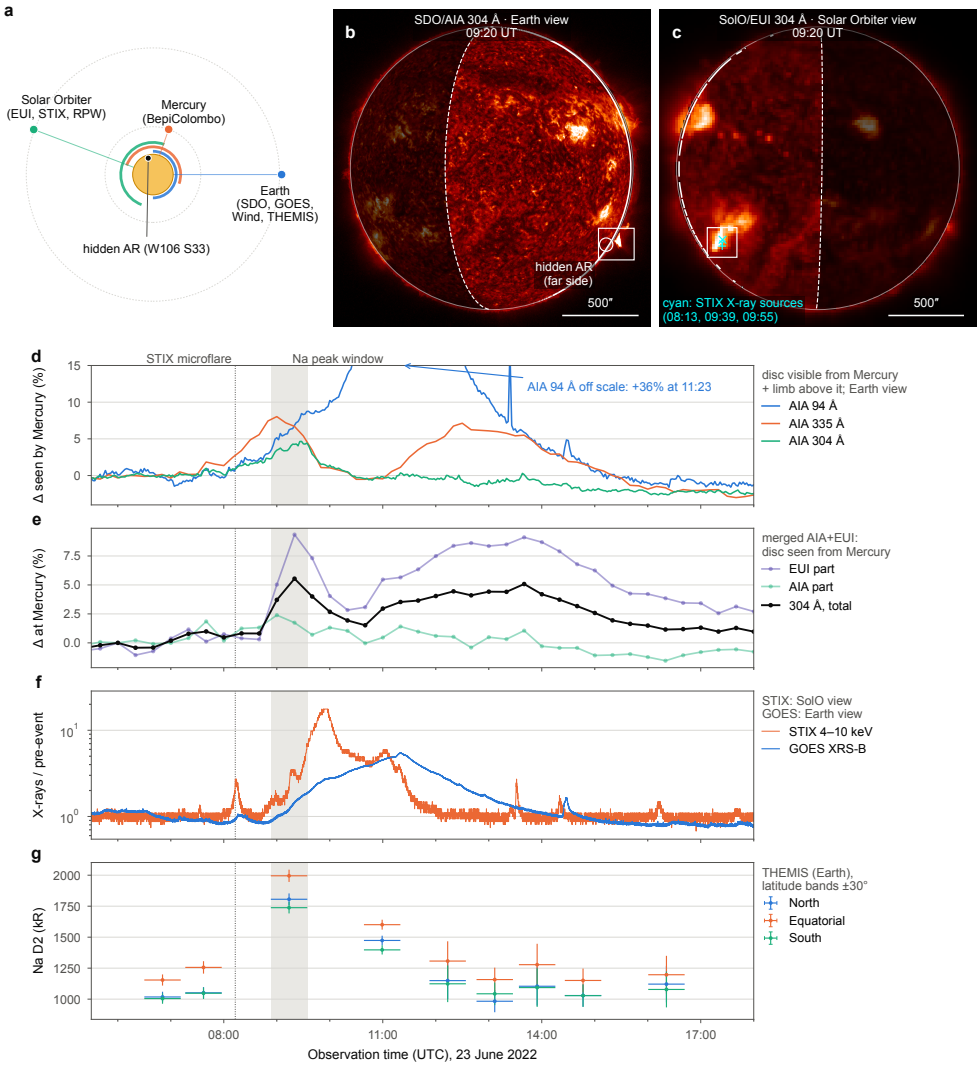


Fig. 5 a) Ecliptic plane view of Earth (W0; 1.016 au), Mercury (W71, 0.378 au) and Solar Orbiter (W159, 1.006 au). Coloured arcs mark the solar longitudes visible from each observer. The black dot is the active region (AR) at W106S33: it is visible from Mercury and Solar Orbiter but 14° behind the west limb as seen from Earth. b) SDO/AIA 304 Å image at 09:20 UT (Earth view). The white box marks the off-limb emission above the south-west limb; the open circle is the projected position of the hidden AR. c) Solar Orbiter/EUI-FSI 304 Å image at 09:20 UT (Solar Orbiter view). The white box encloses the AR; cyan symbols are the STIX X-ray sources of 08:13, 09:39 and 09:55 UT. In b) and c), dimmed areas are not visible from Mercury. d) Percentage change of the full-disk EUV emission: AIA 94, 335 and 304 Å over the part of the solar disk visible from Mercury, plus the off-limb emission above the west limb, which includes the coronal emission of the AR behind it. e) Percentage change of the 304 Å irradiance at Mercury, from AIA and EUI images reprojected onto the view from Mercury and merged (black); purple and green are the contributions of the parts of the disk taken from EUI (including the AR) and from AIA, respectively. f) STIX 4–10 keV count rate and GOES-16 XRS-B 0.1–0.8 nm flux, as ratios to their pre-event levels. Grey shading marks the peak Na brightness. g) Na D2 emission measured by THEMIS in three latitude bands (north, >30°; equatorial, |latitude| $\leq$ 30°; south, < −30°).

In detail, the activity of the AR developed as follows:

- *08:06–08:38 UT.* This interval falls within the THEMIS data gap during which the Na emission starts to increase. A microflare peaks in the STIX 4–10 keV band at 08:13 UT, at 2.7 times the pre-event count rate (4-s cadence); STIX imaging places it at W106 S33, in the AR. The 10–15 keV band peaks at the same time (1.5 times the pre-event rate), while no significant emission is detected above 15 keV. The X-ray peak is accompanied by a type III radio burst recorded by Solar Orbiter/RPW, drifting from ∼2.4 MHz at 08:13 UT to ∼140 kHz at 08:28 UT, which traces electron beams escaping from the flare site along open magnetic field lines. The burst is not detected by Wind/WAVES or STEREO-A/WAVES (not shown), which are separated from the AR by 106° and 132° in longitude, compared with 53° for Solar Orbiter, consistent with the directivity of type III emission [e.g. 40]. The coincidence of the X-ray peak with the type III burst marks the impulsive phase of the flare in the AR. During the impulsive phase, energy deposition by accelerated electrons in the chromosphere typically enhances the far- and near-UV emission (UV continuum, Lyman-α) at the flare footpoints [e.g. 41, 42]. Such an enhancement, if present, is not observable here. As seen from Earth, the AR lies 14.4° beyond the west limb, so that only structures higher than $R_\odot(1/\cos 14.4° - 1) \approx 23$ Mm are visible above the limb, well above the chromosphere and transition region (a few Mm) where the impulsive-phase UV emission originates. For this reason, we disregarded 1600 and 1700 Å AIA passbands. Solar Orbiter, which sees the AR on the disk, has no far- or near-UV observations of the source region during the event. The only imager observing the AR, EUI/FSI, works in the EUV; its He II 304 Å channel, formed in the upper chromosphere and transition region, is the closest available tracer of impulsive-phase footpoint emission, but its 20-min cadence (frames at 08:00 and 08:20 UT) does not resolve the impulsive phase.
- *08:53–09:34 UT (Na peak, exposure t011).* The STIX 4–10 keV emission rose again, with a sub-peak at 09:17 UT (3.4 times the pre-event level). The 304 Å irradiance at Mercury, computed from the merged Solar Orbiter/EUI and SDO/AIA images of the disk seen from Mercury, increased by 3.7% at 09:00 and 5.5% at 09:20 UT; the part of the disk observed by EUI, which contains the AR, increased by ∼9.5% (Fig. 5e, purple line). From Earth, the off-limb 304 Å emission above the south-west limb rose from about 08:55 UT and peaked at about 09:30 UT (Fig. 5d, green curve), in coincidence with an erupting prominence. Note that in the mosaic the AIA part (Fig. 5e, green curve) is almost flat because only on-disk emission is considered to avoid to count twice the emission from the AR that is already taken into account by EUI.
- *09:34–11:20 UT.* STIX recorded two peaks from the same AR, at 09:39 and 09:55 UT, with GOES-equivalent classes C1.5 and C2.1 estimated from STIX. The 4-10 keV count rate reached its maximum, 18 times the pre-event level, at about 09:54 UT. A third peak followed at 11:04 UT. The gradual soft X-ray phase seen by GOES-16 XRS-B peaked (×5.5) at about 11:21 UT (Fig. 5f). The AIA 94 Å emission integrated over full field of view peaked (+36%) at the same time, mostly from post-flare loops rising above the west limb (Fig. 5d). Over this interval, the Na emission decreased (exposure t016).

- *After 11:20 UT.* The 304 Å emission of the AR remained about 3–5% above the pre-event level until about 14:00 UT, owing to the post-flare loops, and returned to close the pre-event level after about 16:00 UT. Na emission returns to its initial level earlier, from about 12:46 UT (exposure t024) onward.

Therefore, the impulsive phase of the AR, marked by the microflare, took place in the THEMIS gap during which the Na emission started to increase, and the subsequent EUV brightening of the AR, seen from Solar Orbiter, was simultaneous with the Na peak (Fig. 5e,g). The Na increase involved the whole dayside: the north, equatorial and south bands increased by factors of 1.75, 1.66 and 1.69, respectively, and decreased together (Fig. 5g). The decay of the Na emission took place while the X-ray emission was reaching its maximum and the post-flare EUV emission of the AR was still enhanced.

3 Discussion

Considering together all the multi-messenger observations available during MFB2, we can state that:

i) The plasma conditions at Mercury cannot be the primary responsible of the Na intensification. In fact, BepiColombo showed that the solar wind energy was nearly stable. The upstream magnetic field was fluctuating producing potentially enhanced reconnection rate, but we can exclude that the ion or electron precipitation onto Mercury's day side surface was the cause of the sudden increase of Na exosphere observed between 8:53 and 9:35 on 23 June 2022. BepiColombo/SIXS-P did not record any solar energetic particles upstream of the magnetosphere but only a local magnetospheric electron signal.

ii) The Na increase involved the whole day side, with nearly identical relative increases in the northern, equatorial and southern bands (factors 1.75, 1.66, 1.69, respectively), and the three bands decreased together. A uniform relative response is what is expected from a release process driven globally, like solar irradiance.

iii) A dominant solar activity directed toward Mercury is registered before and during the Na intensification. This is surely related to the Na release.

iv) The solar activity continued also during the Na recovery phase, indicating that the surface release process is not just a simple cause-effect relation, but a complex mechanism should be considered.

v) An increase of the g-factor (the efficiency of an atom to emit at the specific wavelength [e.g. 43]) is also unlikely; it depends on solar flux at the Na D lines, and the white-light continuum does not change appreciably during C-class flares.

The dominant solar activity directed towards Mercury during the event was that of the AR hidden from Earth. Its impulsive phase (08:10–08:30 UT) occurred in the THEMIS data gap within which the Na emission started to rise, and the EUV brightening of the AR seen by Solar Orbiter was simultaneously with the Na peak. The later (09:39–11:04 UT) and stronger X-ray flares of the same AR, and the 304 Å EUV emission due to post-flare loops, occurred while the Na emission was already decreasing. If PSD is the dominant release process, the photons involved are mainly in the 4–10 eV range (1250–3000 Å) [8], for which no observations of the source region are available

because the source is located 14° behind the limb (so that the transition region and the chromosphere are not visible) with respect to SDO/AIA, while Solar Orbiter does not provide observations in the UV range during this event. The relative change of the Na emission exceeds the measured change of the EUV irradiance at Mercury (+6% at 304 Å) by about an order of magnitude; this would require either a larger relative change in the unobserved FUV–NUV range, or a release efficiency increasing faster than linearly with the photon flux, as suggested by lunar observations [20]. However, PSD depends on the integral of the solar spectrum $\phi_{ph}(\lambda)$:

$$\phi_{Na} = \frac{1}{4} N_{Na} \int \phi_{ph}(\lambda)\sigma(\lambda)d\lambda, \tag{1}$$

where ϕ_{Na} and $\phi_{\mathrm{ph}}(\lambda)$ are the Na released flux and the impinging photon flux at λ wavelength, respectively, N_{Na} is the Na concentration onto the surface and $\sigma(\lambda)$ is the wavelength-dependent cross section of the process. From such an analysis the nonlinearity of the efficiency for EUV-PSD process cannot be proved, which in contrast can simply be an indirect relation due to the fact that the EUV, especially at 304Å (which tracks the upper chromosphere and transition region emission, so that it is the closest available tracer of impulsive-phase footpoint emission), covaries with potential UV bands enhancement. Nevertheless, a full-disk variability of FUV–NUV fluxes is not expected to be greater than a few percent.

To explain a Na response much larger than the relative change of EUV irradiance, a more complex mechanism should be invoked, as in the case of chemical sputtering that enhances the PSD efficiency [14]. Considering the infrequent high-energy (EUV) photons arriving at the surface with respect to UV and white-light continuum, a multi-phase process could be hypothesized, which is sketched in Fig. 6. Before the flare (Fig. 6a), the exosphere is sustained by steady release processes, mainly near-UV PSD acting on the Na adsorbed on the grain surfaces, while the grains contain a pool of Na that is bound in the mineral and cannot be desorbed directly. In a first phase (Fig. 6b), the EUV photons of the flare, which penetrate the uppermost tens of nanometres of the grains, break the bonds in the mineral and make part of this pool available on the grain surfaces. The released atoms do not need to be desorbed by the EUV photons themselves, i.e., once on the surface, they are desorbed by far more numerous NUV photons, whose flux at Mercury makes the residence time of an adsorbed atom of the order of an hour at the subsolar point [8]. In this picture, the scarcity of EUV photons limits the activation of the pool, not the release into the exosphere, and the exospheric response can be delayed with respect to the EUV enhancement by up to about the residence time of the adsorbed atoms. This is consistent with the observed sequence, i.e., the impulsive phase of the AR occurred in the THEMIS gap within which the Na emission started to increase, and the Na emission peaked during the EUV brightening of the AR seen from Solar Orbiter. The atoms falling back to the surface remain available for subsequent releases until they migrate to the night side, are photo-ionized, or are lost from the exosphere via Jeans escape. Since the atom detachment depends mainly on the irradiance, the relative enhancement is expected to be similar across the day side, as observed in the three latitude bands. Possible local variations in mineralogy cannot be excluded, but cannot be identified at the THEMIS image resolution.

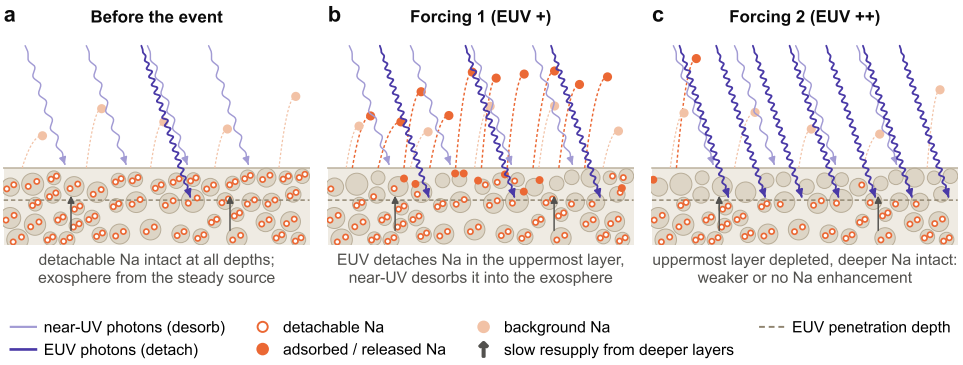


Fig. 6 Schematic of the proposed scenario. a, Before the event, the exosphere is sustained by the steady source (light symbols) and the pool of mineral-bound Na (open circles) is intact and present at all depth. **b**, During a flare, EUV photons penetrate the grains (above the dashed line) and turn bounded Na into adsorbed Na on the grain surfaces (filled circles), which the UV photons desorb into the exosphere; deeper layers are not affected. **c**, The uppermost layer is depleted and only slowly resupplied from the deeper layers, so a later and stronger EUV brightening produces a weaker or no Na enhancement.

The pool of detachable Na is finite and replenished slowly (Fig. 6c). Once it is exhausted, further EUV enhancements (such as in the case of post-flare loops) and later flares find few Na to detach and produce a weaker or negligible enhancement of the exosphere, until the pool is replenished, e.g., by diffusion or resurfacing. The response of the exosphere is therefore not a function of the instantaneous solar irradiance but depends on its recent history, and a flare occurring within a few hours of a previous one is expected to produce a weaker effect. The replenishment time must be at least of the order of the duration of the event, i.e., few hours, for the later flares of the same AR not to produce a visible or weaker response. The pool cannot coincide with the whole Na content of the uppermost layer, which is far larger than the amount released during the event, and should rather consist of Na in weakly bound or defect sites, such as those produced by space weathering.

Two conditions must be met for this scenario to account for the observations. First, the activation must be driven by the flare component of the spectrum rather than by the total EUV flux. Radiation that is weak in the quiet Sun and strongly enhanced in flares, such as soft X-rays and the EUV lines, or a process with a threshold in the irradiance, would satisfy this condition. Second, the pool must be large enough to supply the additional Na released during the event, and small enough to be exhausted by a single event. Repeated observations of the exosphere during sequences of flares from the same active region would test the predicted refractory behavior.

While the EUV emission of the AR seen from Mercury peaked at about 09:20 UT, decreased within the following hour and remained 3–5% above its pre-event level between about 11:00 and 14:00 UT due to post-flare loops, the Na exosphere recovery was much faster, reaching the initial values at about 12:46 UT, about 4 hours after the onset of the increase. The proposed scenario is compatible with the observed recovery

phases of the driver and of the Na exosphere. After a prompt increase in the free Na atoms on the surface, the pool of detached Na in the uppermost layer becomes depleted (Fig. 6c); therefore, in the second phase, the exospheric Na circulation is the leading process that defines the recovery time. According to this scenario, the later EUV enhancement (post flare loops) is no longer able to release additional Na, because the detached pool is replenished only slowly.

This behavior is compatible with a Na exosphere with a sticking probability below 1, i.e. the capacity of the released atom to rebound to the surface, producing bouncing of Na atoms once emitted the first time up to the night side where the atoms rest [44]. A similar effect is obtained considering a sticking probability of 1, but with a low binding energy, resulting in a quick re-emission due to UV radiation [45, 46]. As mentioned above, the gradual decrease of the Na exosphere is then mostly due to the depletion of the detached Na atoms in the upper surface, due to Na segregation on the nightside, to radiation pressure and to loss due to photo-ionization [47].

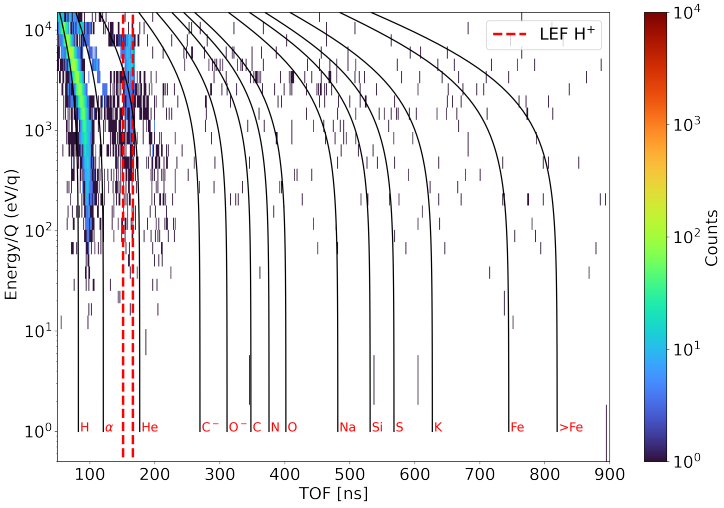


Fig. 7 BepiColombo MSA ToF spectral analysis integrated between 9:33 and 9:49 UT inside Mercury's magnetosphere during MFB2. Black lines show the calibration curves for different species. Linear electric field (LEF) ions induce secondary electrons which signature is observed between the two red dashed lines.

We note that while radiation pressure is proportional to the photons in the visible range (i.e. at the D1 and D2 Na emission lines), the photo-ionization is due to UV photons below 241 nm, partly overlapping with the range of the PSD process. Therefore, the enhanced Na exosphere implies a proportionally enhanced generation of planetary ions by photo-ionization, thus the presence of Na ions circulating in Mercury's magnetosphere is expected. During MFB2, BepiColombo MPPE-MSA mass spectrometer measured protons, He^{++}, He^{+} and traces of heavier ions. The integrated

Time of Flight (ToF) distribution in the time interval between 9:33 and 9:49 UT at CA (Fig. 7) shows that calibration curves match with a Na^+ peak (at 2 keV) and secondary O^+ and K^+ peaks, which supports the Na enhancement during this period. The expected energies of the newly ionized atoms are lower, but the ions may soon begin to circulate and become energized in the magnetosphere [48, 49]. These energies, observed about one hour after the onset of the event, could indicate an acceleration towards the dawn side of the photo-ionized ions on the day side. The data also show an increase in low-energy heavy ions, but these are mostly He^+ and O^+.

4 Conclusion

This study reports the first observation of a transient enhancement of Mercury's Na exosphere coincident with a solar flare directed towards the planet. The PSD process has been considered one of the major causes of Na exosphere generation at Mercury [8, 9, 20], but its short-term variability has never before been associated with solar flare emission. During MFB2, no evidence was found for enhanced particle precipitation; the global day-side-wide character of the enhancement points to a driver acting on the whole illuminated hemisphere. In this case study, a flare, and the subsequent EUV brightening of an active region facing Mercury coincided with a strong, day-side-wide effect on the Na exosphere, whereas later and stronger emissions due to post-flare loops (especially in the X-band) produced no further Na increase. The response of the exosphere is therefore not expected to scale simply with the flare magnitude, but to depend also on the time elapsed since previous events. A statistical study of the Na exosphere ground-based images obtained in the past THEMIS observation campaigns in relation to solar flare occurrence will test this prediction.

The amplitude of the response (~ 70 %), much larger than the relative change of the EUV irradiance measured at Mercury (~ 5.7 %), is reminiscent of the steeper than linear correlation of the lunar Na exosphere on solar EUV reported by Devaraj et al. [20]. Here, we propose a two-phase process (Fig. 6). First, the high energy photons of the flare break the Na bonds in the minerals and make a finite pool of Na available on the grain surfaces; then the far more intense UV-photon flux desorbes these newly adsorbed atoms into the exosphere. The detachable pool of uppermost surface Na atoms is exhausted within the first hour of the event and replenished only slowly. After this first phase, only the Na atoms already circulating between the surface and the exosphere remain available.

This multi-instrument and multi-point observation study is a clear example of the potential of BepiColombo when it will start the nominal mission phase with two spacecraft observing Mercury's environment [50], with the possibility of adding observations from Earth and from other missions in the inner heliosphere. Simultaneous measurements of the X-ray, EUV and UV irradiance of the solar regions facing Mercury would directly identify the radiation driving the release. This study is relevant not only for understanding the interaction of the Sun with Mercury, but also for investigating the effects of solar flare radiation on other airless bodies such as the Moon.

5 Data and Methods

5.1 THEMIS observations

Earth-based data are obtained using the THEMIS solar telescope [51] located in Tenerife (Canaries, Spain). THEMIS is a Ritchey-Chretien telescope with a 15.04 m focal and a 0.9 m primary mirror that is long used during the daylight to image Mercury Na exosphere above the disk, and can operate continuously for several hours per day. THEMIS is equipped with MTR, the MulTiRaies spectrometer in multiline mode [52] that is able to observe at the same time with two different cameras the Na D1 (589.6 nm) and D2 (589.0 nm) lines. More details of the telescope characteristics, configuration and capabilities are widely described in previous papers based on the same dataset [5, 18, 53]. The single full-disk Na image requires about 41 minutes to be completed: each North-South strip of pixels is obtained in a total of 200 s integration time; then the spectrograph slit is shifted in the East-West direction until the end of the scan to cover the full illuminated disk of Mercury.

In this study, we used the D2 emission images obtained on 23 June 2022 between 06:30 and about 16:40 UT where one image (at 9:41) has been excluded for problems in the pointing. The observation campaign continued after MFB2 until 30 June 2022 [24]. To remove background noise, we have considered only the daylight region of the planetary disk within 1.3 R_M. We have removed spikes, defined as pixels whose signal exceeds 3 times the standard deviation relative to their nearest neighboring pixels. The resulting images are reported in Fig. 2. The error (E) of intensity (I) has been considered and calculated as:

$$E = sqrt(I * S)/Q \tag{2}$$

where S is the seeing and Q is a quality factor evaluated according to weather conditions during observations as listed in Table 1. To evaluate exospheric distributions and asymmetries, we considered the emission in three different latitudinal (L) regions: the equatorial region ($abs(L) \leq asin(0.4)$ and the northern/southern regions ($L > asin(0.4)/L < -asin(0.4)$), as reported in Fig. 5.

5.2 BepiColombo Observations

During the BC cruise phase, the SERENA ion sensors (PICAM and MIPA) boresights are oriented in a direction perpendicular to the spacecraft-Sun line. MPPE sensors pointed also perpendicularly to the Sun in a direction perpendicular to the SERENA ion sensors boresights. MOSIF partially obstructs the FoV of the Mio instruments, thus the effective FoV is about 45° . During the planet magnetospheric crossing SERENA ion sensors boresights pointed Northwards, while MPPE FoV pointed Duskwards (Fig. 1).

5.2.1 SERENA-PICAM

Planetary Ion Camera (PICAM) is the ion mass spectrometer of Search for Exospheric Refilling and Emitted Natural Abundances (SERENA) [54]. The PICAM energy range is from a few electronvolts to ~ 3 keV, a mass range extending up to ~ 132 amu, and an instantaneous field of view (FoV) of approximately half sky ($> 1.65\pi$ sr).

During the observations outside Mercury's magnetosphere it was operated in solar wind mode, i.e. without mass resolution and in the energy range of 500–3000 eV (Fig. 3). Given that the boresight is oriented perpendicularly to the Sun, the solar wind can only partially enter the detector, depending on the aberration due to the spacecraft velocity, V_{SC}. The solar wind energy values reported in Table 2 have been obtained averaging the PICAM peak energies in the inbound and outbound periods shown in Fig. 3.

During the magnetospheric interval of MFB2, PICAM operated in full energy range in image mode, i.e. no mass resolution (Fig. 4a).

5.2.2 SERENA-MIPA

Miniature Ion Plasma Analyser (MIPA) is the ion analyser of SERENA [54]. It is a small, configurable plasma analyzer [55] with an approximately 1.9π hemispherical FoV and an energy range of 30 eV–14 keV. The number of pixels and energy bins are configurable onboard the instrument, resulting in varying resolutions with a time of 20 s to scan all possible combinations with an electrostatic deflection system and cylindrical electrostatic analyzer. MIPA is optimized for measurements of very high fluxes of penetrating solar wind in Mercury's magnetosphere, thus the counts in the solar wind (pixels on the edge of the FoV) and in the magnetotail are low.

At MFB2, MIPA was operated with 16 energy bins and 48 pixels [31] (Fig. 4b).

5.2.3 MERMAG

Magnetic field measurements are collected during the cruise phase by the three-axial fluxgate magnetometers onboard the MPO (MPO-MAG) [56] and the Mio spacecraft (Mio-MGF) [57]. Each of the two instruments consists of two identical boom-mounted fluxgates. The MPO-MAG boom was deployed soon after launch, enabling dual-sensor measurements. The Mio-MGF boom will be deployed after the Mio separation. During cruise, the Mio-MGF sensors are stored close to each other and register nearly identical magnetic fields.

During the Mercury's flybys, the measurements of both instruments suffered from artificial magnetic disturbances due to the spacecraft operations and temperature gradients. During MFB2, the AC error increases significantly during the eclipse phase (09:27-09:45) and decreases to similar values after the eclipse, while the DC error increases after the start of the eclipse. The MERMAG data is the cleaned magnetic field obtained after an extended joint analysis of both MPO-MAG and Mio-MGF measurements [33]. Near the closest approach, artificial disturbances cannot be completely removed, resulting in a gap in the plotted data (Fig. 4d).

The resulting IMF measurements are shown in Fig. 3. The IMF magnitude values reported in Table 2 have been obtained averaging the data in the inbound and outbound periods shown in the same figure.

5.2.4 MPPE-MEA

The Mercury Plasma Particle Experiment (MPPE) [58] onboard Mio includes, among other sensors, the Mercury Electron Analyser (MEA) and the Mass Spectrum Analyzer (MSA). MEA is composed by two analyzers, MEA1 and MEA2, but only MEA1 data are used in this study. During MFB2 MEA1 measured electrons in the energy range from 3 eV to 3 keV, with 16 energy bins, and a time resolution of 4 s. The data have been cleaned in the low energy range following the Rojo et al. [28] method. The measurements obtained during MFB2 are shown in Fig. 4c.

5.2.5 MPPE-MSA

MSA is an ion mass spectrum analyzer. It scans 64 energy bins from 1 eV/q to 38 keV/q every 66 s. Here, MSA energy spectra correspond to all particle masses. During the cruise phase, MSA FoV is reduced by the sun-shield from 4 π sr to 0.1 π sr. The observations obtained inside the magnetosphere by MSA and integrated between 9:33 and 9:49 UT during MFB2 are shown in Fig. 7. The data presented in Fig. 7 were treated to remove the noise from accidental counts caused by the saturation of MSA by the intense proton flux. Linear electric field (LEF) ions induce secondary electrons which signature is observed between the two red vertical dashed lines in Fig. 7 [59]. MSA detected an enhancement of O, Na, and K ions with energies of a few keV during its closest approach. He^+ is the main component of the low-energy heavy ions measured during the CA.

5.2.6 SIXS

The Solar Intensity X-ray and particle Spectrometer (SIXS) on board MPO measures the direct solar X-rays, energetic protons, and electrons [60]. SIXS includes three X-ray detectors and a particle detector with five view cones pointing to orthogonal directions. The SIXS sensor unit is located at the corner of the MPO radiator side in such a way that the SIXS-X visibility to the Sun and the SIXS-P visibility to the full sky is good during all the Mercury orbit phases. During the cruise phase, part of the sky is obstructed by the sun-shield of Mio. The sun-shield blocks one of the SIXS-P view cones entirely and another one partly. In particular, during MFB2 the X-Ray sensor toward the Sun was obstructed, thus preventing to observe solar flares.

SIXS-P detects electrons in the nominal energy range from 50 keV to 3 MeV and protons in the range from 1 to 30 MeV. During MFB2, the proton measurements did not show any relevant signal, while the electron signal showed a clear increase at the exit from the shadow when BepiColombo was in the dawn magnetosphere as shown in Fig. 4e.

5.3 Solar emission

5.3.1 Geometry

The heliocentric positions of Mercury, Earth and Solar Orbiter were taken from the JPL Horizons ephemerides. At 09:00 UT, the Stonyhurst longitudes were W70.8 (Mercury, 0.378 au), W0 (Earth, 1.016 au) and W159.3 (Solar Orbiter, 1.006 au). This configuration allowed SDO (Earth view) and Solar Orbiter to observe from opposite sides the solar longitudes facing Mercury. All times in this work are given as recorded by each instrument, without light-travel-time corrections. BepiColombo times refer to the spacecraft at Mercury, THEMIS times to the reception of the Na emission at Earth, and SDO, GOES, Solar Orbiter (EUI, STIX, RPW) and Wind times to the respective observers. Earth and Solar Orbiter were at nearly the same heliocentric distance (1.016 and 1.006 au), so that they record the same solar signal within ∼5 s. The solar radiation reached Mercury $(r_{\rm obs} - r_{\rm M})/c \approx 5.2$ min before it was recorded at 1 au, and the Na emission observed by THEMIS left Mercury $d_{\rm ME}/c \approx 8.0$ min before its detection. The net offset between the solar and THEMIS time series is therefore ≈3 min, negligible with respect to the 41-min THEMIS exposures.

5.3.2 EUV light curves

We used all SDO/AIA [61] level-1 images at 94, 335 and 304 Å of 23 June 2022 (12-s cadence) (http://jsoc.stanford.edu/) and the level-2 304 Å images of the Full Sun Imager (FSI) of Solar Orbiter/EUI [62] (20-min cadence) (https://sidc.be/EUI/data/L2/). AIA frames with a non-zero quality flag were discarded, and each frame was divided by its exposure time. No detector-background subtraction was applied.

For Fig. 5d, we summed the AIA signal over the on-disk pixels whose surface point lies within 90° of the sub-Mercury point, i.e., the part of the hemisphere facing Mercury that is visible from Earth. To this we added all off-limb pixels on the west side of the image, i.e., the limb facing Mercury. The off-limb pixels are needed because the AR, 14° behind the west limb, is seen from Earth only through its coronal emission above the limb. The mask was computed from the image WCS and the ephemerides, and updated every 2 h, which is sufficient because the sub-Mercury point moves by less than 1° in the instrument frame over the day.

For Fig. 5e, we computed the 304 Å irradiance at Mercury from simultaneous AIA and EUI images. For each EUI frame, we took the AIA frame closest to it in time at Mercury (within 3 min). We converted both images into radiance. For AIA, we used the wavelength response at 303.8 Å, including the time-dependent degradation and the EVE cross-calibration [63, 64]. For EUI, we used a calibration factor obtained by cross-calibrating EUI on AIA in the quiet Sun at disk centre. Both radiance maps were reprojected onto the view from Mercury, assuming that the emission lies on the solar surface, so off-limb structures are not retained. Each point of the hemisphere visible from Mercury was taken from the instrument that sees it closer to disk centre (larger μ), which avoids double counting. The irradiance at Mercury is the sum of the merged radiance times the solid angle of each pixel as seen from Mercury. In Fig. 5e, the EUI and AIA contributions are the sums over the points taken from each instrument; the

AR lies in the part taken from EUI. Frames for which the merged map covered less than 95% of the visible disk were discarded.

5.3.3 X-ray and radio observations

We used the STIX [65] quick-look light curves (4-s cadence) in the 4–10, 10–15 and 15–25 keV bands, and the GOES-16 XRS-B 1-s fluxes, discarding flagged data. Flare times, positions and GOES-equivalent classes estimated from STIX were taken from the STIX flare list [66, 67]. Since the AR is behind the limb as seen from Earth, the GOES classes measured at Earth do not represent the flare emission. Radio bursts were identified in the Solar Orbiter/RPW [68] dynamic spectra (TNR and HFR receivers) and searched for in Wind/WAVES and STEREO-A/WAVES. In Fig. 5d–f, all light curves are expressed relative to their median over 06:00–07:30 UT.

Acknowledgements. The THEMIS telescope is operated through the French-Spanish Laboratory for Astrophysics in Canarias (FSLAC; CNRS & IAC) on the island of Tenerife, Spain, and yearly funded by the French Centre National de la Recherche Scientifique - Institut National des Sciences de l'Univers (CNRS-INSU). The authors acknowledge the THEMIS staff for their fruitful help and support throughout the many years of Mercury's observation.
SERENA is supported by the Italian Space Agency (ASI) and by the Italian National Institute of Astrophysics (INAF): SERENA agreement no. 2024-66-HH.0 "Attività scientifiche per il Payload SERENA su BepiColombo, relative alla fine della fase di crociera e fase operativa". The MIPA sensor was developed with support from the Swedish National Space Agency, the Swedish Institute of Space Physics, and the University of Bern. PICAM and MGF were developed with support from the Austrian Research Promotion Agency (FFG) and the Programme de Développement d'Expériences scientifiques (PRODEX).
D.H. was supported by the German Ministerium für Wirtschaft und Klimaschutz and the German Zentrum für Luft und Raumfahrt under contract 50QW2202.
The French participation in the BepiColombo mission is funded by the Centre National d'Etudes Spatiales (CNES).
EK and RV acknowledge the financial support of the Research Council of Finland (SOLMER, grants 361480 and 361483; SpaceResilience, grants 374096 and 374097).
Work at MPS is funded by the Federal Ministry of Research, Technology and Space (BMFTR) through the German Space Agency at DLR on the basis of a resolution of the German Bundestag (Funding codes: 50QW2501, 50QW2101, 50QW1702, 50QW1303, 50QW0503) and by the Max Planck Society.

References

[1] Leblanc, F., Schmidt, C., Mangano, V., Mura, A., Cremonese, G., Raines, J., Jasinski, J., Sarantos, M., Milillo, A., Killen, R., *et al.*: Comparative na and k mercury and moon exospheres. Space Science Reviews **218**(1), 2 (2022)

[2] Leblanc, F., Schmidt, C., Mangano, V., Mura, A., Cremonese, G., Raines, J.M., Jasinski, J.M., Sarantos, M., Milillo, A., Killen, R.M., *et al.*: Comparative Na and K Mercury and Moon exospheres. In: Milillo, A., Sarantos, M., Teolis, B., Murakami, G., Wurz, P. (eds.) Surface-Bounded Exospheres and Interactions in the Inner Solar System. Space Sciences Series of ISSI, vol. 84, pp. 213–268. Springer, Dordrecht (2024). https://doi.org/10.1007/s11214-022-00871-w

[3] Cassidy, T.A., McClintock, W.E., Killen, R.M., Sarantos, M., Merkel, A.W., Vervack Jr, R.J., Burger, M.H.: A cold-pole enhancement in mercury's sodium exosphere. Geophysical Research Letters **43**(21), 11–121 (2016)

[4] Milillo, A., Mangano, V., Massetti, S., Mura, A., Plainaki, C., Alberti, T., Ippolito, A., Ivanovski, S.L., Aronica, A., De Angelis, E., *et al.*: Exospheric na distributions along the mercury orbit with the themis telescope. Icarus **355**, 114179 (2021)

[5] Massetti, S., Mangano, V., Milillo, A., Mura, A., Orsini, S., Plainaki, C.: Short-term observations of double-peaked na emission from mercury's exosphere. Geophysical Research Letters **44**(7), 2970–2977 (2017)

[6] Orsini, S., Mangano, V., Milillo, A., Plainaki, C., Mura, A., Raines, J.M., De Angelis, E., Rispoli, R., Lazzarotto, F., Aronica, A.: Mercury sodium exospheric emission as a proxy for solar perturbations transit. Scientific reports **8**(1), 928 (2018)

[7] Mura, A., Milillo, A., Mangano, V., Leblanc, F., Moroni, M., Massetti, S., Richards, G., Plainaki, C., Brin, A., De Angelis, E., et al.: Hot poles at mercury from micro-meteoroids weathering. Earth, Planets and Space (2026)

[8] Wurz, P., Fatemi, S., Galli, A.e.a.: Particles and photons as drivers for particle release from the surfaces of the moon and mercury. Space Science Reviews **218**(10) (2022)

[9] Wurz, P., Fatemi, S., Galli, A., Halekas, J., Harada, Y., Jäggi, N., Jasinski, J., Lammer, H., Lindsay, S., Nishino, M.N., Orlando, T.M., Raines, J.M., Scherf, M., Slavin, J., Vorburger, A., Winslow, R.: Particles and photons as drivers for particle release from the surfaces of the Moon and Mercury. In: Milillo, A., Sarantos, M., Teolis, B., Murakami, G., Wurz, P. (eds.) Surface-Bounded Exospheres and Interactions in the Inner Solar System. Space Sciences Series of ISSI, vol. 84, pp. 5–87. Springer, Dordrecht (2024). https://doi.org/10.1007/s11214-022-00875-6

[10] Verkercke, S., Morrissey, L., Chaufray, J., Georgiou, A., Ricketts, A., Leblanc, F.: On the origins of mercury's sodium exospheric cold poles enhancement: A multi-scale exosphere global model. Journal of Geophysical Research: Planets **130**(11), 2025–009309 (2025)

[11] Killen, R.M., Morrissey, L.S., Burger, M.H., Vervack Jr, R.J., Tucker, O.J., Savin,

D.W.: The influence of surface binding energy on sputtering in models of the sodium exosphere of mercury. The Planetary Science Journal **3**(6), 139 (2022)

[12] Jäggi, N., Biber, H., Brötzner, J., Szabo, P., Stefan Mutzke, A., Gasser, J., Aumayr, F., Wurz, P., Galli, A.: Spubase: Solar wind ion sputter database for modeling purposes. The Planetary Science Journal **5**, 75 (2024)

[13] Morrissey, L.S., Lewis, J., Ricketts, A., Berhanu, D., Bu, C., Dong, C., al.: Theoretical calculations on the effect of adsorbed atom coverage on the sodium exospheres of airless bodies. The Astrophysical Journal **981**(1), 73 (2025) https://doi.org/10.3847/1538âĂŘ4357/adad63

[14] Mura, A., Wurz, P., Lichtenegger, H.I., Schleicher, H., Lammer, H., Delcourt, D., Milillo, A., Orsini, S., Massetti, S., Khodachenko, M.L.: The sodium exosphere of mercury: Comparison between observations during mercury's transit and model results. Icarus **200**(1), 1–11 (2009)

[15] Killen, R., Morgan, T.: Diffusion of na and k in the uppermost regolith of mercury. Journal of Geophysical Research: Planets **98**(E12), 23589–23601 (1993)

[16] Killen, R., Potter, A., Reiff, P., Sarantos, M., Jackson, B., Hick, P., Giles, B.: Evidence for space weather at mercury. Journal of Geophysical Research: Planets **106**(E9), 20509–20525 (2001)

[17] Mangano, V., Massetti, S., Milillo, A., Mura, A., Orsini, S., Leblanc, F.: Dynamical evolution of sodium anisotropies in the exosphere of mercury. Planetary and Space Science **82**, 1–10 (2013)

[18] Mangano, V., Massetti, S., Milillo, A., Plainaki, C., Orsini, S., Rispoli, R., Leblanc, F.: Themis na exosphere observations of mercury and their correlation with in-situ magnetic field measurements by messenger. Planetary and Space Science **115**, 102–109 (2015)

[19] Solomon, S.C., Nittler, L.R., Anderson, B.J. (eds.): Mercury: The View After MESSENGER. Cambridge Planetary Science, vol. 21. Cambridge University Press, Cambridge (2018)

[20] Devaraj, A., Narendranath, S., Kartha, S.S., Sarantos, M., Akhil, K.R., Mathew, B., Sivarani, T., Nidhi, S., Anbazhagan, P., Selvakumar, G.: Non-linear solar euv-driven sodium release from the lunar surface: a contrast to the linear psd model. Monthly Notices of the Royal Astronomical Society **543**(2), 1079–1091 (2025) https://doi.org/10.1093/mnras/staf1447

[21] Yakshinskiy, B.V., Madey, T.E.: Photon-stimulated desorption as a substantial source of sodium in the lunar atmosphere. https://doi.org/10.1038/23204. Nature **400**, 642–644 (1999) https://doi.org/10.1038/23204

[22] Woods, T.N., Hock, R., Eparvier, F., Jones, A.R., Chamberlin, P.C., Klimchuk, J.A., Didkovsky, L., Judge, D., Mariska, J., Warren, H., Schrijver, C.J., Webb, D.F., Bailey, S., Tobiska, W.K.: New Solar Extreme-ultraviolet Irradiance Observations during Flares. **??**jnlApJ **739**(2), 59 (2011) https://doi.org/10.1088/0004-637X/739/2/59

[23] Benkhoff, J., Murakami, G., Baumjohann, W., Besse, S., Bunce, E., Casale, M., Cremosese, G., Glassmeier, K.-H., Hayakawa, H., Heyner, D., *et al.*: Bepicolombo-mission overview and science goals. **??**jnlSSRv **217**(8), 90 (2021)

[24] Mangano, V., Massetti, S., Milillo, A., ...: Mercury Na exosphere during the BepiColombo flybys 2, 3 and 4, as seen from ground-based telescopes. Submitted to the BepiColombo Special Issue on EPS (2026)

[25] Shue, J.-H., Chao, J., Fu, H., Russell, C., Song, P., Khurana, K., Singer, H.: A new functional form to study the solar wind control of the magnetopause size and shape. Journal of Geophysical Research: Space Physics **102**(A5), 9497–9511 (1997)

[26] Winslow, R.M., Anderson, B.J., Johnson, C.L., Slavin, J.A., Korth, H., Purucker, M.E., Baker, D.N., Solomon, S.C.: Mercury's magnetopause and bow shock from messenger magnetometer observations. Journal of Geophysical Research: Space Physics **118**(5), 2213–2227 (2013)

[27] Di Bartolomeo, P.P., Stumpo, M., Benella, S., Alberti, T., Milillo, A., Varsani, A., Heyner, D., Aronica, A., Jeszenszky, H., Kazakov, A., *et al.*: Detecting in situ directional discontinuities in the solar wind at mercury's orbit. Astronomy & Astrophysics **700**, 55 (2025)

[28] Rojo, M., André, N., Aizawa, S., Sauvaud, J.-A., Saito, Y., Harada, Y., Fedorov, A., Penou, E., Barthe, A., Persson, M., Yokota, S., Mazelle, C., Hadid, L.Z., Delcourt, D., Fontaine, D., Fränz, M., Katra, B., Krupp, N., Murakami, G.: Structure and dynamics of the hermean magnetosphere revealed by electron observations from the mercury electron analyzer after the first three mercury flybys of bepicolombo. Astronomy & Astrophysics **687**, 243 (2024)

[29] Teubenbacher, D., Exner, W., Narita, Y., Varsani, A., Schmid, D., Jeszenszky, H., Laky, G., Fischer, D., Baumjohann, W., Matsuoka, A., *et al.*: Hybrid modeling of mercury's magnetosphere: Assessing accuracy in ion counting statistics. Astronomy & Astrophysics **698**, 12 (2025)

[30] Schmid, D., Varsani, A., al.: Ongoing magnetic reconnection at Mercury's Magnetotail, detected by BepiColombo. submitted to Journal of Geophysical Research: Space (2026)

[31] Williamson, H.N., Barabash, S., Nilsson, H., Wieser, M., Raines, J.M., Milillo, A., Varsani, A., Aronica, A., DeAngelis, E., Futaana, Y., *et al.*: Bepicolombo

at mercury: Three flybys, three magnetospheres. Geophysical Research Letters **53**(2), 2025–119589 (2026)

[32] Delcourt, D., Hadid, L., Aizawa, S.: On the response of protons to dynamical reconfigurations of mercury's magnetosphere. Geophysical Research Letters **51**(21), 2024–110351 (2024)

[33] Constantinescu, O.D., Auster, H., Fischer, D., Herčík, D., Heyner, D., Plaschke, F., Richter, I., Magnes, W.: Disturbance-aligned-frame gradiometer technique for removal of spacecraft-generated disturbances from the bepicolombo magnetic field data. Earth, Planets and Space **78**(1), 16 (2026)

[34] Aizawa, S., Harada, Y., André, N., Saito, Y., Barabash, S., Delcourt, D., Sauvaud, J.-A., Barthe, A., Fedorov, A., Penou, E., *et al.*: Direct evidence of substorm-related impulsive injections of electrons at mercury. Nature Communications **14**(1), 4019 (2023)

[35] Dewey, R.M., Slavin, J.A., Raines, J.M., Baker, D.N., Lawrence, D.J.: Energetic Electron Acceleration and Injection During Dipolarization Events in Mercury's Magnetotail. Journal of Geophysical Research (Space Physics) **122**(12), 12170–12188 (2017) https://doi.org/10.1002/2017JA024617

[36] Cushen, A.T., Sun, W., Slavin, J., Dewey, R., Jia, X., Zhao, J.: Dipolarization regions in mercury's magnetosphere: Observation of flux pileup and formation of a substorm current wedge. Geophysical Research Letters **52**(24), 2025–117281 (2025) https://doi.org/10.1029/2025GL117281 https://agupubs.onlinelibrary.wiley.com/doi/pdf/10.1029/2025GL117281. e2025GL117281 2025GL117281

[37] Teubenbacher, D., Exner, W., Feyerabend, M., Narita, Y., Schmid, D., Laky, G., Toepfer, S., Motschmann, U., Bourdin, P.-A., Comişel, H.: Solar wind entry into mercury's magnetosphere: Simulation results for the second swingby of bepicolombo. Astronomy & Astrophysics **681**, 98 (2024)

[38] Lavorenti, F., Jensen, E.A., Aizawa, S., Califano, F., d'Amore, M., Domingue, D., Henri, P., Lindsay, S., Raines, J.M., Savin, D.W.: Maps of solar wind plasma precipitation onto mercury's surface: A geographical perspective. The Planetary Science Journal **4**(9), 163 (2023)

[39] Killen, R.M., McLain, J.L., Burger, M.H., Tucker, O.J., Morrissey, L.S., Vervack Jr, R.J.: An estimate of the importance of electron-stimulated desorption of sodium at mercury. The Planetary Science Journal **6**(7), 160 (2025)

[40] Bonnin, X., Hoang, S., Maksimovic, M.: The directivity of solar type III bursts at hectometer and kilometer wavelengths: Wind-Ulysses observations. **??**jnlA&A **489**(1), 419–427 (2008) https://doi.org/10.1051/0004-6361:200809777

[41] Fletcher, L., Dennis, B.R., Hudson, H.S., Krucker, S., Phillips, K., Veronig, A., Battaglia, M., Bone, L., Caspi, A., Chen, Q., Gallagher, P., Grigis, P.T., Ji, H., Liu, W., Milligan, R.O., Temmer, M.: An Observational Overview of Solar Flares. **??**jnlSSRv **159**(1-4), 19–106 (2011) https://doi.org/10.1007/s11214-010-9701-8 arXiv:1109.5932 [astro-ph.SR]

[42] Li, D., Lu, L., Ning, Z., Feng, L., Gan, W., Li, H.: Quasi-periodic Pulsation Detected in Lyα Emission During Solar Flares. **??**jnlApJ **893**(1), 7 (2020) https://doi.org/10.3847/1538-4357/ab7cd1 arXiv:2003.01877 [astro-ph.SR]

[43] Potter, A.E., Killen, R.M., Morgan, T.H.: Solar radiation acceleration effects on mercury sodium emission. Icarus **186**(2), 571–580 (2007)

[44] Leblanc, F., Johnson, R.E.: Mercury exosphere i. global circulation model of its sodium component. Icarus **209**(2), 280–300 (2010)

[45] Mura, A.: Loss rates and time scales for sodium at mercury. Planetary and Space Science **63**, 2–7 (2012)

[46] Morrissey, L.S., Tucker, O.J., Killen, R.M., Nakhla, S., Savin, D.W.: Solar wind ion sputtering of sodium from silicates using molecular dynamics calculations of surface binding energies. The Astrophysical Journal Letters **925**(1), 6 (2022)

[47] Jasinski, J.M., Cassidy, T.A., Raines, J.M., Milillo, A., Regoli, L.H., Dewey, e.a. R.: Photoionization loss of mercury's sodium exosphere: Seasonal observations by messenger and the themis telescope. Geophysical Research Letters **48**, 2021–092980 (2021)

[48] Delcourt, D.C., Grimald, S., Leblanc, F., Berthelier, J.-J., Millilo, A., Mura, A., Orsini, S., Moore, T.E.: A quantitative model of the planetary Na+ contribution to Mercury's magnetosphere. Annales Geophysicae **21**(8), 1723–1736 (2003) https://doi.org/10.5194/angeo-21-1723-2003

[49] Exner, W., Simon, S., Heyner, D., Motschmann, U.: Influence of Mercury's Exosphere on the Structure of the Magnetosphere. Journal of Geophysical Research (Space Physics) **125**(7), 27691 (2020) https://doi.org/10.1029/2019JA027691

[50] Milillo, A., Fujimoto, M., Murakami, G., Benkhoff, J., Zender, J., Aizawa, S., Dósa, M., Griton, L., Heyner, D., Ho, G., *et al.*: Investigating mercury's environment with the two-spacecraft bepicolombo mission. Space science reviews **216**(5), 93 (2020)

[51] López Ariste, A., Rayrole, J., Semel, M.: First results from THEMIS spectropolarimetric mode. Astronomy and Astrophysics Supplement Series **142**, 137–148 (2000) https://doi.org/10.1051/aas:2000144

[52] Mein, P., Rayrole, J.: Themis solar telescope. Vistas in Astronomy **28**, 567 (1985)

https://doi.org/10.1016/0083-6656(85)90077-7

[53] Leblanc, F., Doressoundiram, A., Schneider, N., Mangano, V., López Ariste, A., Lemen, C., Gelly, B., Barbieri, C., Cremonese, G.: High latitude peaks in mercury's sodium exosphere: Spectral signature using themis solar telescope. Geophysical Research Letters **35**(18) (2008)

[54] Orsini, S., Livi, S., Lichtenegger, H., Barabash, S., Milillo, A., De Angelis, E., Phillips, M., Laky, G., Wieser, M., Olivieri, A., *et al.*: Serena: particle instrument suite for determining the sun-mercury interaction from bepicolombo. Space science reviews **217**(1), 11 (2021)

[55] Wieser, M., Barabash, S.: A family for miniature, easily reconfigurable particle sensors for space plasma measurements. Journal of Geophysical Research: Space Physics **121**(12), 11–588 (2016)

[56] Heyner, D., Auster, H.-U., Fornaçon, K.-H., Carr, C., Richter, I., Mieth, J.Z.D., Kolhey, P., Exner, W., Motschmann, U., Baumjohann, W., Matsuoka, A., Magnes, W., Berghofer, G., Fischer, D., Plaschke, F., Nakamura, R., Narita, Y., Delva, M., Volwerk, M., Balogh, A., Dougherty, M., Horbury, T., Langlais, B., Mandea, M., Masters, A., Oliveira, J.S., Sánchez-Cano, B., Slavin, J.A., Vennerstrøm, S., Vogt, J., Wicht, J., Glassmeier, K.-H.: The BepiColombo Planetary Magnetometer MPO-MAG: What Can We Learn from the Hermean Magnetic Field? Space Science Reviews **217**(4), 52 (2021) https://doi.org/10.1007/s11214-021-00822-x

[57] Baumjohann, W., Matsuoka, A., Narita, Y., Magnes, W., Heyner, D., Glassmeier, K.-H., Nakamura, R., Fischer, D., Plaschke, F., Volwerk, M., *et al.*: The bepicolombo–mio magnetometer en route to mercury. Space Science Reviews **216**(8), 125 (2020)

[58] Saito, Y., Delcourt, D., Hirahara, M., Barabash, S., André, N., Takashima, T., Asamura, K., Yokota, S., Wieser, M., Nishino, M.N., *et al.*: Pre-flight calibration and near-earth commissioning results of the mercury plasma particle experiment (mppe) onboard mmo (mio). Space Science Reviews **217**(5), 70 (2021)

[59] Delcourt, D., Saito, Y., Leblanc, F., Verdeil, C., Yokota, S., Fraenz, M., Fischer, H., Fiethe, B., Katra, B., Fontaine, D., Illiano, J.-M., Berthelier, J.-J., Krupp, N., Buhrke, U., Bubenhagen, F., Michalik, H.: The mass spectrum analyzer (msa) on board the bepicolombo mmo. Journal of Geophysical Research: Space Physics **121**(7), 6749–6761 (2016) https://doi.org/10.1002/2016JA022380 https://agupubs.onlinelibrary.wiley.com/doi/pdf/10.1002/2016JA022380

[60] Huovelin, J., Vainio, R., Kilpua, E., Lehtolainen, A., Korpela, S., Esko, E., Muinonen, K., Bunce, E., Martindale, A., Grande, M., *et al.*: Solar intensity x-ray and particle spectrometer sixs: instrument design and first results. Space Science Reviews **216**(5), 94 (2020)

[61] Lemen, J.R., Title, A.M., Akin, D.J., Boerner, P.F., Chou, C., Drake, J.F., Duncan, D.W., Edwards, C.G., Friedlaender, F.M., Heyman, G.F., *et al.*: The atmospheric imaging assembly (aia) on the solar dynamics observatory (sdo). In: Chamberlin, P., Pesnell, W.D., Thompson, B. (eds.) The Solar Dynamics Observatory, pp. 17–40. Springer, New York, NY (2012)

[62] Rochus, P., Auchère, F., Berghmans, D., Harra, L., Schmutz, W., Schühle, U., Addison, P., Appourchaux, T., Aznar Cuadrado, R., Baker, D., Barbay, J., Bates, D., BenMoussa, A., Bergmann, M., Beurthe, C., Borgo, B., Bonte, K., Bouzit, M., Bradley, L., Büchel, V., Buchlin, E., Büchner, J., Cabé, F., Cadiergues, L., Chaigneau, M., Chares, B., Choque Cortez, C., Coker, P., Condamin, M., Coumar, S., Curdt, W., Cutler, J., Davies, D., Davison, G., Defise, J.-M., Del Zanna, G., Delmotte, F., Delouille, V., Dolla, L., Dumesnil, C., Dürig, F., Enge, R., François, S., Fourmond, J.-J., Gillis, J.-M., Giordanengo, B., Gissot, S., Green, L.M., Guerreiro, N., Guilbaud, A., Gyo, M., Haberreiter, M., Hafiz, A., Hailey, M., Halain, J.-P., Hansotte, J., Hecquet, C., Heerlein, K., Hellin, M.-L., Hemsley, S., Hermans, A., Hervier, V., Hochedez, J.-F., Houbrechts, Y., Ihsan, K., Jacques, L., Jérôme, A., Jones, J., Kahle, M., Kennedy, T., Klaproth, M., Kolleck, M., Koller, S., Kotsialos, E., Kraaikamp, E., Langer, P., Lawrenson, A., Le Clech', J.-C., Lenaerts, C., Liebecq, S., Linder, D., Long, D.M., Mampaey, B., Markiewicz-Innes, D., Marquet, B., Marsch, E., Matthews, S., Mazy, E., Mazzoli, A., Meining, S., Meltchakov, E., Mercier, R., Meyer, S., Monecke, M., Monfort, F., Morinaud, G., Moron, F., Mountney, L., Müller, R., Nicula, B., Parenti, S., Peter, H., Pfiffner, D., Philippon, A., Phillips, I., Plesseria, J.-Y., Pylyser, E., Rabecki, F., Ravet-Krill, M.-F., Rebellato, J., Renotte, E., Rodriguez, L., Roose, S., Rosin, J., Rossi, L., Roth, P., Rouesnel, F., Roulliay, M., Rousseau, A., Ruane, K., Scanlan, J., Schlatter, P., Seaton, D.B., Silliman, K., Smit, S., Smith, P.J., Solanki, S.K., Spescha, M., Spencer, A., Stegen, K., Stockman, Y., Szwec, N., Tamiatto, C., Tandy, J., Teriaca, L., Theobald, C., Tychon, I., van Driel-Gesztelyi, L., Verbeeck, C., Vial, J.-C., Werner, S., West, M.J., Westwood, D., Wiegelmann, T., Willis, G., Winter, B., Zerr, A., Zhang, X., Zhukov, A.N.: The Solar Orbiter EUI instrument: The Extreme Ultraviolet Imager. **??**jnlA&A **642**, 8 (2020) https://doi.org/10.1051/0004-6361/201936663

[63] Boerner, P., Edwards, C., Lemen, J., Rausch, A., Schrijver, C., Shine, R., Shing, L., Stern, R., Tarbell, T., Title, A., Wolfson, C.J., Soufli, R., Spiller, E., Gullikson, E., McKenzie, D., Windt, D., Golub, L., Podgorski, W., Testa, P., Weber, M.: Initial Calibration of the Atmospheric Imaging Assembly (AIA) on the Solar Dynamics Observatory (SDO). **??**jnlSoPh **275**(1-2), 41–66 (2012) https://doi.org/10.1007/s11207-011-9804-8

[64] Barnes, W., Cheung, M., Bobra, M., Boerner, P., Chintzoglou, G., Leonard, D., Mumford, S., Padmanabhan, N., Shih, A., Shirman, N., Stansby, D., Wright, P.: aiapy: A Python Package for Analyzing Solar EUV Image Data from AIA. The Journal of Open Source Software **5**(55), 2801 (2020) https://doi.org/10.21105/joss.02801

[65] Krucker, S., Hurford, G.J., Grimm, O., Kögl, S., Gröbelbauer, H.-P., Etesi, L., Casadei, D., Csillaghy, A., Benz, A.O., Arnold, N.G., Molendini, F., Orleanski, P., Schori, D., Xiao, H., Kuhar, M., Hochmuth, N., Felix, S., Schramka, F., Marcin, S., Kobler, S., Iseli, L., Dreier, M., Wiehl, H.J., Kleint, L., Battaglia, M., Lastufka, E., Sathiapal, H., Lapadula, K., Bednarzik, M., Birrer, G., Stutz, S., Wild, C., Marone, F., Skup, K.R., Cichocki, A., Ber, K., Rutkowski, K., Bujwan, W., Juchnikowski, G., Winkler, M., Darmetko, M., Michalska, M., Seweryn, K., Białek, A., Osica, P., Sylwester, J., Kowalinski, M., Ścisłowski, D., Siarkowski, M., Stęślicki, M., Mrozek, T., Podgórski, P., Meuris, A., Limousin, O., Gevin, O., Le Mer, I., Brun, S., Strugarek, A., Vilmer, N., Musset, S., Maksimović, M., Fárník, F., Kozáček, Z., Kašparová, J., Mann, G., Önel, H., Warmuth, A., Rendtel, J., Anderson, J., Bauer, S., Dionies, F., Paschke, J., Plüschke, D., Woche, M., Schuller, F., Veronig, A.M., Dickson, E.C.M., Gallagher, P.T., Maloney, S.A., Bloomfield, D.S., Piana, M., Massone, A.M., Benvenuto, F., Massa, P., Schwartz, R.A., Dennis, B.R., van Beek, H.F., Rodríguez-Pacheco, J., Lin, R.P.: The Spectrometer/Telescope for Imaging X-rays (STIX). **??**jnlA&A **642**, 15 (2020) https://doi.org/10.1051/0004-6361/201937362

[66] Xiao, H., Maloney, S., Krucker, S., Dickson, E., Massa, P., Lastufka, E., Francesco Battaglia, A., Etesi, L., Hochmuth, N., Schuller, F., Ryan, D.F., Limousin, O., Collier, H., Warmuth, A., Piana, M.: The data center for the Spectrometer and Telescope for Imaging X-rays (STIX) on board Solar Orbiter. **??**jnlA&A **673**, 142 (2023) https://doi.org/10.1051/0004-6361/202346031 arXiv:2302.00497 [astro-ph.SR]

[67] stix: STIX data center — stix,. [Online; accessed 12-October-2026] (2022). https://pub023.cs.technik.fhnw.ch/wiki/index.php?title=STIX_data_center&oldid=16171

[68] Maksimovic, M., Bale, S.D., Chust, T., Khotyaintsev, Y., Krasnoselskikh, V., Kretzschmar, M., Plettemeier, D., Rucker, H.O., Souček, J., Steller, M., Štverák, Š., Trávníček, P., Vaivads, A., Chaintreuil, S., Dekkali, M., Alexandrova, O., Astier, P.-A., Barbary, G., Bérard, D., Bonnin, X., Boughedada, K., Cecconi, B., Chapron, F., Chariet, M., Collin, C., de Conchy, Y., Dias, D., Guéguen, L., Lamy, L., Leray, V., Lion, S., Malac-Allain, L.R., Matteini, L., Nguyen, Q.N., Pantellini, F., Parisot, J., Plasson, P., Thijs, S., Vecchio, A., Fratter, I., Bellouard, E., Lorfèvre, E., Danto, P., Julien, S., Guilhem, E., Fiachetti, C., Sanisidro, J., Laffaye, C., Gonzalez, F., Pontet, B., Quéruel, N., Jannet, G., Fergeau, P., Brochot, J.-Y., Cassam-Chenai, G., Dudok de Wit, T., Timofeeva, M., Vincent, T., Agrapart, C., Delory, G.T., Turin, P., Jeandet, A., Leroy, P., Pellion, J.-C., Bouzid, V., Katra, B., Piberne, R., Recart, W., Santolík, O., Kolmašová, I., Krupař, V., Krupařová, O., Píša, D., Uhlíř, L., Lán, R., Baše, J., Ahlèn, L., André, M., Bylander, L., Cripps, V., Cully, C., Eriksson, A., Jansson, S.-E., Johansson, E.P.G., Karlsson, T., Puccio, W., Břínek, J., Öttacher, H., Panchenko, M., Berthomier, M., Goetz, K., Hellinger, P., Horbury, T.S., Issautier, K., Kontar, E., Krucker, S., Le Contel, O., Louarn, P., Martinović, M., Owen, C.J., Retino, A., Rodríguez-Pacheco, J.,

971 Sahraoui, F., Wimmer-Schweingruber, R.F., Zaslavsky, A., Zouganelis, I.: The
972 Solar Orbiter Radio and Plasma Waves (RPW) instrument. **??**jnlA&A **642**, 12
973 (2020) https://doi.org/10.1051/0004-6361/201936214